

Electric Field-Driven Dielectrophoretic Elastomer Actuators

Ciqun Xu, Charl F. J. Faul, Majid Taghavi,* and Jonathan Rossiter*

Dielectrophoresis is the electro-mechanical phenomenon where a force is generated on a dielectric material when exposed to a non-uniform electric field. It has potential to be exploited in smart materials for robotic manipulation and locomotion, but to date it has been sparsely studied in this area. Herein, a new type of dielectrophoretic actuator exploiting a novel electroactive polymer is described, termed as dielectrophoretic elastomer (DPE), which undergoes electric field-driven actuation through dielectrophoresis. Unique deflection and morphing behavior of the elastomer induced by controlling the dielectrophoretic phenomenon, such as out-of-plane deformation and independence of electric field polarity, are illustrated. The dielectric and mechanical properties of the DPE are studied to gain insight into the influence of materials composition on deformation. Actuation performance using different electrode parameters is experimentally investigated with supplementary analysis through finite element simulation, revealing the relationship between electric field inhomogeneity and deflection. The applications of DPE actuators in a range of robotic devices is demonstrated, including a pump, an adjustable optical lens, and a walking robot. This diverse range of applications illustrates the wide potential of these new soft-and-smart electric field-driven materials for use in soft robotics and soft compliant devices.

creating possibilities for a wide range of applications across manufacturing, manipulation, healthcare, rescue, and human interaction.^[1–4] Advances in soft robotics are significantly accelerated by advances in stimuli-responsive soft materials, which should provide high-performance sensing and actuation while endowing the robots with desired compliance and adaptability. Electroactive polymers have been widely used as muscle-like smart materials in soft robotics, transforming electric stimuli into desired actuation patterns.^[5–7] Among the physical phenomena used in electroactive polymers, electrostatic pressure has been shown to produce high power-density and high energy-density artificial muscles.^[8] Dielectric elastomer actuators, for example, are capable of generating fast, strong, and accurate actuation in response to high voltage electric signals.^[9–13] The soft elastomer layer, sandwiched between two stretchable electrodes, shows biaxial displacement contracting in the thickness direction and expanding in the film

plane direction when a voltage is applied to compliant electrodes. Electro-ribbon actuators, on the other hand, exploit electrostatic forces to zip two insulated electrodes together with a high force amplification achieved by the application of a bead of dielectric liquid at the zipping point.^[14] Hydraulically amplified self-healing electrostatic (HASEL) actuators use electrostatic force to pressurize dielectric liquid in a pouch, and the consequent hydraulic force is utilized for actuation.^[15,16] In addition, electrostatic actuators have also been applied in constructing lenses,^[17] generators,^[18] pumps,^[19] flying robots,^[20] and haptic sleeves^[21] because of their simple structure and electrical controllability.

In the above examples, electrostatic forces act upon the dielectric through direct electrode contact; thus, the movement of the elastomer or dielectric liquid is defined by, and confined by, the electrode. Actuation is achieved by the deformation or displacement of electrodes, and therefore flexible or compliant electrodes are needed, resulting in a complicated fabrication process. In contrast, magnetic force, another fast-response actuation strategy, can provide more freedom and actuation capabilities to magnetically responsive materials without direct magnet contact.^[22] By concentrating a magnetic field in a certain space, actuation materials can move freely in any direction without the constrain of direct magnetic contact. Nevertheless, to generate a strong enough and controllable magnetic field even in a tiny actuation space, a bulky and power consuming external magnetic control system is needed.^[23,24]

1. Introduction


Soft robots have received growing attention due to their ability to interact compliantly with humans and environments,

C. Xu, J. Rossiter
Department of Engineering Mathematics
University of Bristol
Bristol BS8 1TW, UK
E-mail: jonathan.rossiter@bristol.ac.uk

C. Xu, J. Rossiter
Bristol Robotics Laboratory
Bristol BS16 1QY, UK

C. F. J. Faul
School of Chemistry
University of Bristol
Bristol BS8 1TS, UK

M. Taghavi
Department of Bioengineering
Imperial College London
London SW7 2AZ, UK
E-mail: m.taghavi@imperial.ac.uk

 The ORCID identification number(s) for the author(s) of this article can be found under <https://doi.org/10.1002/adfm.202208943>.

© 2023 The Authors. Advanced Functional Materials published by Wiley-VCH GmbH. This is an open access article under the terms of the Creative Commons Attribution License, which permits use, distribution and reproduction in any medium, provided the original work is properly cited.

DOI: 10.1002/adfm.202208943

Dielectrophoresis is a field-derived phenomenon and has been studied in detail since the first work of Pohl in the 1950s.^[25–28] As illustrated in Figure S1 (Supporting Information), a dielectrophoretic force acts upon a dielectric material inside an inhomogeneous electric field. The electrodes and dielectric can be separated, providing fewer constraints to the movement and deformation of the dielectric. On the other hand, the generation of the electric field does not require bulky and compliant electrodes (in contrast to the high current windings needed for magnetic field manipulation and the compliant electrodes required in dielectric elastomer actuators), which results in simple fabrication and a more flexible design space. The use of dielectrophoresis therefore enables potentially more controllable, direct, and facile electromechanical transduction and morphing capabilities in soft materials.

Dielectrophoresis has been explored to manipulate the motion of electrically polarized particles and liquid droplets.^[29–31] Owing to the field-driven features, it has been proved to be powerful in particle manipulation and widely employed in applications of microfluidics,^[32] cell separation,^[33] drug delivery,^[34] dielectric liquid lenses,^[35,36] microwire assembly,^[37,38] and has recently been used in soft electronics to aligning liquid metal microdroplets in an elastomer matrix.^[39] Dielectrophoresis is also exploited to pull dielectric liquid beads into the zipping point of electro-ribbon actuators, resulting in a significant reduction in the mass of the actuators.^[14] However, dielectrophoretic forces have not been used to drive artificial muscles directly; rather dielectrophoresis has been serendipitously used to support the main direct-contact electrostatic attraction force.^[14] Mainstream uses of dielectrophoresis focus on manipulating nano/micro-particles but ignore the behavior of bulk materials, mainly because the interaction with small size objects is more effective. The premise has been that scaling down the dimensions of matter endows a large surface-to-volume ratio, thus a relatively large surface area for interaction can be obtained. Nevertheless, dielectrophoresis is highly dependent on the electric field gradient and properties of materials, which provide opportunities for interaction with, and development of, new elastomeric polymers targeted at the dielectrophoretic phenomenon.

Here, we introduce a new class of electroactive material, termed a dielectrophoretic elastomer (DPE), which is the first-ever demonstrated active morphing and moving matter that is driven by inhomogeneities in the electric field. The DPE, when placed between a circular electrode (A) and an annular electrode (B), as shown in **Figure 1a i**, deforms in a perpendicular direction due to the spatially inhomogeneous electric field. This DPE actuator exhibits out-of-plane deflection, which is a challenge for counterpart technologies. For example, dielectric elastomer actuators without utilizing a transmission mechanism, such as incorporating a constraining layer^[40,41] or inhomogeneous electrodes,^[42] Although the deformation of dielectric elastomer actuators under inhomogeneous electric fields has been studied,^[43] the actuation principle still relies on compressing the sandwiched elastomer layer via Maxwell stress. By comparison, Maxwell stress also works as the fundamental mechanism behind dielectrophoresis,^[44,45] but the deformation or locomotion of elastomers in dielectrophoretic actuators is achieved by stretching or pulling. The principal comparison

between these two actuators is discussed under Figure S2 (Supporting Information). The easy fabrication of our DPE actuator and its versatile functionality allows it to be integrated into various practical devices. In this paper, we explore its potential for applications in pumps, optical lenses, and walking robots. Our DPE approach demonstrates a high potential to push the frontiers of artificial muscle technologies and provide new solutions for the design of soft and compliant devices.

2. Results and Discussion

2.1. Principle of Dielectrophoretic Elastomer Actuators

As a proof of concept, we illustrated the different behavior of the DPE when subjected to a uniform and a non-uniform electric field respectively created by parallel plate electrodes (Figure S3, Supporting Information). In Video S1 and Figure S4 (Supporting Information), the DPE remains stationary in the uniform electric field but morphs when the field is non-uniform. The polarity of electric field does not affect the deformation direction of the DPE. The results indicate that the inhomogeneity of electric field is required for DPE deformation, revealing the dominating role of dielectrophoresis. Further, dielectrophoresis can not only deform the DPE but also control its locomotion. As demonstrated in Video S2 and Figure S5 (Supporting Information), a DPE strip suspended between – but not touching – two electrodes, can move in the air toward one of the electrodes where a voltage is applied. This control strategy avoids direct electrode contact, thus enabling significant freedom of movement without any mechanical constraints from the electrodes. This is analogous to magnetic field actuation but using an electric field, opening the door to a wide range of new electric actuation possibilities.

To further investigate the interaction of electric field and our solid dielectrophoretic elastomers, we designed prototype DPE actuators using the parameterized electrode structure (Figure 1a i; Figure S6, Supporting Information). Because the structure of a typical DPE actuator is axisymmetric, the half sectional view could be simplified as a circular aperture geometry (Figure 1a ii). It is important to note that there is an air gap between Electrode A and the DPE, which is different from the sandwich structure of dielectric elastomer actuators. The established electric field is determined by the geometry of electrodes, and we emphasize three parameters related to electrodes in this paper: the diameter of Electrode A (D_A), the inner diameter of Electrode B (D_B), and distance between two electrodes (D_C), which will be investigated in Section 2.3. In order to harness dielectrophoresis for actuation, understanding the relationship between dielectrophoresis and the electric field is necessary. Figure 1b is a Finite Element simulation of voltage distribution (left) and the corresponding electric field strength distribution (right) conducted in COMSOL Multiphysics (see Experimental Section for detailed simulation parameters). There are two options when applying a voltage to the electrodes: connecting either Electrode A (I) or Electrode B (II) to the higher electrical potential. The resultant electric fields I and II have inverse field directions (left side of Figure 1b), but their field strength distribution is identical (right side of Figure 1b). Unless otherwise

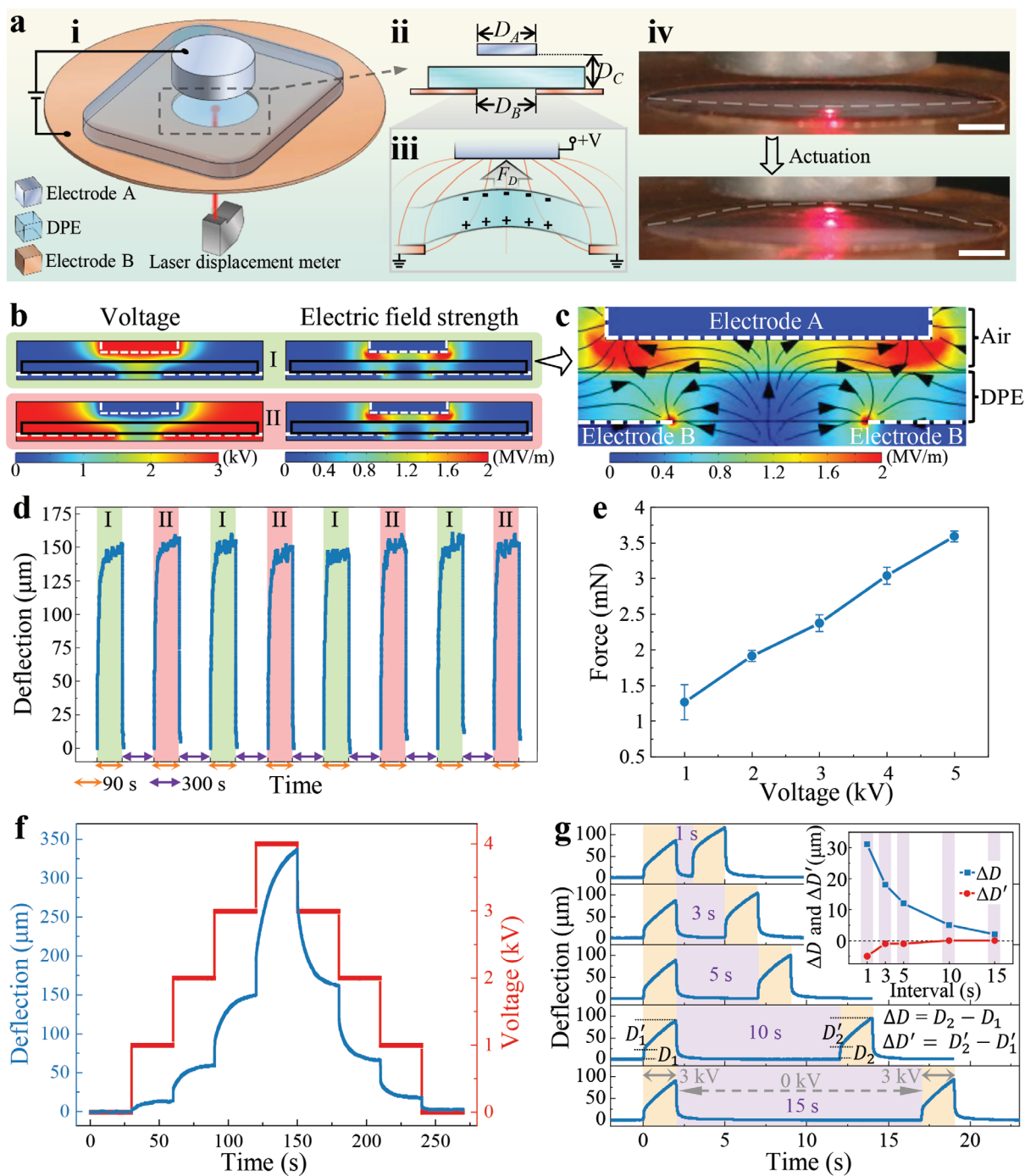


Figure 1. Design, principle, and performance of DPE actuators. a) i: Schematic diagram of a simple DPE actuator with a cylindrical electrode (top), a DPE in the middle, and an annular electrode (bottom). A laser displacement meter underneath is used to measure the deflection of the DPE. ii: Diagram of the cross-sectional view of the DPE actuator. Three essential electrode parameters D_A , D_B , and D_C represent the diameter of Electrode A, the inner diameter of Electrode B, and the distance between two electrodes, respectively. iii: Actuation principle. When applying a voltage to the electrode, a non-uniform electric field is formed, leading to the polarization of DPE and the generation of dielectrophoretic force (F_D). iv: An example of actuation with electrode parameters of $D_A = 10$ mm, $D_B = 15$ mm, and $D_C = 2.5$ mm. Scale bar is 2 mm. b) Finite element simulation of the voltage (left) and electric field strength (right) distribution at a voltage of 3 kV. For easy recognition, the boundaries of electrodes and DPE are depicted with white dash lines and black solid lines, respectively. c) A zoomed-in illustration of the result in the top-right of (b). Black arrows are simulation results of electric field magnitude gradient. d) Deflection comparison of actuation under two reversed electric fields. The electric fields I (top electrode positive) and II (top electrode negative) correspond to I and II in (b), respectively. e) Actuation force generated by the DPE at different driving voltages. f) Deflection at different driving voltages. g) Influence of the interval between electrical stimulations on the deflection. Each actuation cycle takes 2 s at 3 kV, and intervals vary from 1 to 15 s. Insert shows the change of ΔD and $\Delta D'$ depending on intervals. Electrode parameters in b) – g) are $D_A = 10$ mm, $D_B = 6$ mm, and $D_C = 2.5$ mm, except $D_A = 15$ mm, $D_B = 15$ mm, and $D_C = 2.5$ mm in e).

specified, we employ field I for actuation in this paper. Owing to the annular structure of Electrode B, field strength distribution is inhomogeneous between the sides and center area of the DPE actuator, which is the key to creating dielectrophoresis. The dielectrophoretic force (F_D) can be expressed as,^[29,46]

$$F_D \propto [CM](E \cdot \nabla) E \quad (1)$$

where E is the electrical field, ∇ represents the gradient operator of vector calculus, and $[CM]$ denotes a Clausius-Mossotti function. The magnitude of F_D is proportional to electric field intensity and gradient, while the polarity is determined by the $[CM]$. The value of $[CM]$ is related to the polarizability of materials and given by,

$$CM = \left(\frac{\epsilon_p - \epsilon_m}{\epsilon_p + 2\epsilon_m} \right) \quad (2)$$

where ϵ_p and ϵ_m represent the relative permittivity of the actuation material and the surrounding medium, respectively.^[47] In our case, the DPE ($\epsilon_p = 2.8$) is actuated in air ($\epsilon_m = 1$) and the polarizability of the DPE is greater than air ($\epsilon_p > \epsilon_m$), so that $[CM]$ has a positive value, leading to the positive dielectrophoresis.^[29,32] In other words, the DPE membrane is always attracted to regions of stronger electric field.

A zoomed-in view of the electric field strength simulation is shown in Figure 1c. A stronger electric field exists in the air region, especially around the corners of Electrode A, whereas the center area possesses a weaker electric field. Black arrows illustrate the field gradient direction (from weak to strong), which also reveals the direction of F_D because the polarity of F_D complies with the field gradient according to Equation 1. Maxwell stress can also indicate the distribution of F_D , as Maxwell stress is usually integrated into dielectrophoretic force calculation.^[44,45] Finite element simulation of Maxwell stress is shown in Figure S7 (Supporting Information). More stress distributes around the side area of the suspended DPE, which means the side area is more active at the beginning of actuation. As the electric field is axisymmetric, the resultant F_D can be simplified as a force that is perpendicular to the DPE membrane toward Electrode A (Figure 1aiii). An example of actuation is illustrated in Figure 1aiv and an image of the actuator is shown in Figure S6 (Supporting Information). Upon applying a voltage, the DPE membrane morphs from a concave into a convex profile as it is attracted towards the high electric field around Electrode A. More details are shown in Figure S8a and Video S3a (Supporting Information).

The dielectrophoretic force is independent of electric field direction.^[28] We demonstrate this property by actuating the DPE under two identical, but opposite electric fields, as shown in Figure 1d. The applied electric fields I and II are the same in magnitude (at a voltage of 3 kV) but reversed in direction, and are consistent with the simulated fields in Figure 1b I and II, respectively. Each actuation cycle takes 90 s under fields I and II alternately, and a 300 s interval is employed between each cycle to avoid influence between cycles. Although fields I and II are switched several times, the deflection behavior is unaffected, reaching $\approx 150 \mu\text{m}$ within 90 s. This result is because I and II have the same electric field strength distribution (Figure 1b),

and the electric field gradient is essential to dielectrophoresis, rather than the electric field direction. This further supports the hypothesis that dielectrophoresis is the dominant driving force in this new class of actuator.

As explained by Equation 1, electric field intensity (E) has a direct influence on dielectrophoretic driving force (F_D), so a straightforward way to enhance dielectrophoretic driving force is to increase the voltage. As illustrated in Figure 1e, the actuation force grows linearly from 1.26 mN at 1 kV to 3.59 mN at 5 kV (measurement detail is shown in Figure S9, Supporting Information). The specific energy density of the system also observes an increasing tendency, reaching 393 J m^{-3} at 5 kV (Figure S10, Supporting Information). Additionally, we measured the areal strain of the DPE based on its out-of-plane deformation (Figure S11, Supporting Information); a result of 1.0% with a strain rate of $0.016\% \text{ s}^{-1}$ is obtained. By comparison, although dielectric elastomer actuators can produce larger output force (0.25 – 686 mN),^[48] higher energy density ($100 - 500 \text{ kJ m}^{-3}$),^[49] and large strain (15%),^[40] they require high amplitude of stimulus ($100 - 150 \text{ kV mm}^{-1}$).^[50] The actuation of the DPE actuator can be achieved by an electric field of only 1.2 kV mm^{-1} (approximately two orders of magnitude lower than dielectric elastomers) since at least one of the electrodes is separated from the active membrane. Besides, soft electromagnetic actuator counterparts can generate large forces, for example, a soft helical coil bending actuator can generate 32 mN.^[51] However, the input power reaches 1 W, which is approximately two orders of magnitude higher than the DPE actuator ($< 0.018 \text{ W}$). Resistance forces, including mechanical stiffness of DPE and gravitational force, also affect the actuation response. Actuation of the DPE occurs when the driving force is greater than the resistive forces. The relationship between actuation deflection and voltage is depicted in Figure 1f, where deflection is boosted or suppressed simultaneously with the increase or decrease of voltage. The dielectrophoretic force is increased when the voltage rises, while the resistive force is unchanged at this instance; therefore, the deflection grows sharply in the beginning. The DPE is gradually deformed and stretched, which increases the mechanical stiffness of the DPE, reducing the difference between driving resistance and driving force until equilibrium is reached. The reverse occurs when decreasing voltage. This is the reason why the deflection curve tends to become stable when the voltage is kept constant.

DPEs exhibit a “memory” effect, as depicted in Figure 1g. Two actuation cycles (2 s for each, at 3 kV) are applied, with an interval in the range 1 to 15 s. D_1 and D_1' are defined as the deflection during the 0 – 0.1 s and 0.1 – 2 s periods of the first cycle, while D_2 and D_2' represent the deflection of the second cycle during the 0 – 0.1 s and 0.1 – 2 s periods, as labeled in the subgraph of Figure 1g. $\Delta D (= D_2 - D_1)$ and $\Delta D' (= D_2' - D_1')$ are used to reveal the deflection difference between the two actuation cycles. The values of D_1 , D_1' , D_2 , D_2' , ΔD , and $\Delta D'$ are listed in Table S1 (Supporting Information). As shown in the inset of Figure 1g, ΔD decreased from 31 to $2 \mu\text{m}$ when the interval was increased from 1 to 15 s, while in comparison, $\Delta D'$ is stable at ≈ 0 . This means that the interval between successive actuation cycles influences the deflection in 0 – 0.1 s of the second cycle, especially when the interval is $< 10 \text{ s}$; the shorter the interval, the more evident the effect. We attribute

this effect to the remnant polarization of the DPE, which can be further proved by the results of an additional experiment (Figure S12, Supporting Information). Interfacial polarization is an important type of polarization especially in a multicomponent system, and the relaxation of polarization may take a few seconds.^[52,53] The interval can be regarded as the time for depolarization process. If the interval is short and the second cycle starts while residual polarization from the first cycle remains, less time is needed for polarization in the second cycle. Thus, the DPE with remnant polarization can be actuated easier, showing larger deflection. It should be noted that polarization is a fast process, and the discussion of the polarization effect is confined to the beginning of actuation (within 0.1 s). This effect is present in AC actuation but is insignificant for DC actuation. On the other hand, actuation relaxation is independent of the polarization and depolarization process, as it happens when the driving voltage is switched off and the electric field disappears. The DPE shows extremely fast actuation relaxation (relaxation rate is 95% in 1 s, Table S1, Supporting Information), which can be further utilized to achieve vibration actuation under square-wave voltage input, as demonstrated in Figure S8b,c and Video S3b (Supporting Information).

2.2. Characterization of Dielectrophoretic Elastomers

Dielectrophoretic actuation raises three basic requirements for materials: i) Electrical polarizability. Polarization of materials is a precondition for dielectrophoresis. ii) High electrical breakdown strength. High electric fields are needed for

dielectrophoresis operation and therefore, the elastomer should possess a high breakdown strength to ensure that a high electric field can be sustained. iii) Low Young's modulus. A low stiffness results in larger deformation. Toward these ends, we developed a series of DPE gels using an elastomer gel (Ecoflex Gel, Smooth-on) and silicone oil. The Ecoflex Gel is a commercially available silicone rubber and compatible with silicone oil. We used a simple one-step method to fabricate the DPE gel by mixing two components without further treatment (see detail in the Experimental Section). Properties of the DPE gels can be tuned by modulating the mixing ratio of the components. Here, we fabricated four DPE gel samples with a silicone oil content of 10, 30, 50, and 70 wt.%, and labeled them as G10, G30, G50, and G70 respectively. A sample of Ecoflex Gel was also prepared with no added silicone oil for comparison.

The dielectric constant at 10 kHz of different samples is shown in Figure 2a, and frequency dependency curves are depicted in Figure S13 (Supporting Information). The difference in oil content does not affect the dielectric constant significantly, with results ranging from 2.6 to 2.8 (as the dielectric constants of two components, Ecoflex Gel (2.6) and silicone oil (2.7) are similar^[14]). Nonetheless, the dielectric constant of DPE samples is more than twice that of air, which provides opportunities for positive dielectrophoresis (discussed in Section 2.1). Figure 2b is the Weibull distribution of electric breakdown strength. The characteristic breakdown strength experiences a decrease with the increase of oil content; for example, 9.2 MV m⁻¹ for G70 compared with 17.6 MV m⁻¹ for Ecoflex Gel. This is probably because more interfaces between oil and elastomer are created in high oil content samples, as

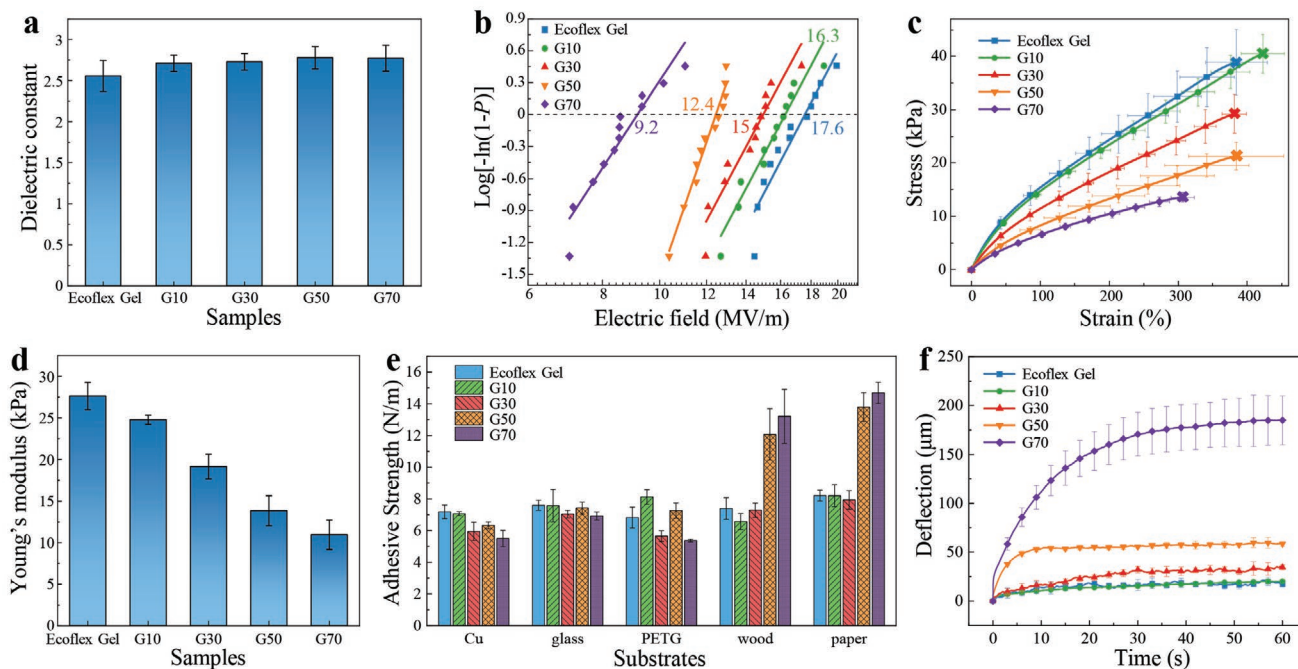


Figure 2. Characterization of DPE with different silicone oil content. a) Dielectric constant measured at 10 kHz. b) Weibull distribution of electrical breakdown strength. P is the cumulative probability of electric failure. Solid lines are fitted results according to experimental data. Displayed numbers are characteristic breakdown strengths of each sample, corresponding to a 63.2% probability of failure. c) Stress–strain curves. d) Young's modulus. e) Interfacial adhesive strength to various substrates. f) Comparison of actuation performance at 3 kV, using electrode parameters of $D_A = 10$ mm, $D_B = 6$ mm, and $D_C = 2.5$ mm.

elastomer networks are surrounded by silicone oil. In a strong enough electric field, those interfaces are more likely to cause charge accumulation, resulting in an electric breakdown. It is noteworthy that the breakdown strength of G70 is still three times greater than air, indicating its ability to work as a DPE actuator, which needs to withstand high voltages for dielectrophoresis operation.

Stress–strain curves of Ecoflex Gel and DPE with different oil ratios are shown in Figure 2c. The method, data acquisition and analysis process of the tensile test is described and discussed in Experimental Section, Figures S14 and S15 (Supporting Information). The Young's moduli in Figure 2d are calculated from the stress–strain curves. A decrease in Young's modulus from Ecoflex Gel (276 kPa) is observed when the sample possesses a higher oil fraction, although breaking elongation of all samples is $\approx 300\%$ to 400% , indicating good stretchability. In particular, G70 exhibits an ultimate tensile strength of 13 kPa, a breaking elongation of 306%, and a Young's modulus of only 11 kPa. Each DPE sample is composed of an oil phase and an elastomeric network, and the mechanical properties mainly come from the latter. The oil content effectively dilutes the elastomeric network in the DPE, thus leading to a decrease in Young's modulus. Figure S16 (Supporting Information) further demonstrates the softness and stretchability of DPE. A flat membrane of G70 with 2 cm diameter and 1.5 mm thickness is readily inflated to a large balloon, and recovers to its flat form when the inflation pressure is removed.

90° peeling tests were performed to investigate the adhesive properties of DPE, as shown in Figure 2e (see Figure S17, Supporting Information for photographs of testing setup and substrates). The DPE gels display adhesive strengths from 5 to 21 N m^{-1} on various substrates, including copper (Cu), glass, polyethylene terephthalate glycol (PETG), wood, and paper. The relatively high adhesion of G50 and G70 to paper and wood may result from the low Young's moduli of these samples and the rough surface of the testing substrates, which causes a relatively large contact area between samples and substrates. These adhesive properties enable DPE to adhere to Electrode B firmly without any further fixing procedures, ensuring convenient actuator fabrication and application, which will be mentioned in Section 2.4.

Figure 2f presents the actuation performance of different DPE samples at a voltage of 3 kV with electrode parameters of $D_A = 10 \text{ mm}$, $D_B = 6 \text{ mm}$, and $D_C = 2.5 \text{ mm}$. The performance of G70 is best, increasing sharply at the beginning and gradually reaching $\approx 185 \mu\text{m}$ in 60 s. In comparison, the deflection of G50 ($60 \mu\text{m}$) is far less than G70, while Ecoflex Gel and G10 are almost unaffected by the applied electric field. The actuation speed of G70 is 10 times greater than Ecoflex Gel (Figure S18, Supporting Information). We primarily attribute the difference in actuation to the difference in Young's modulus. As G70 has a lower Young's modulus than other samples, weaker mechanical stresses are generated against the dielectrophoretic force during the actuation process. Therefore, G70 always shows the greatest actuation performance, even if at different actuation voltages (Figure S19, Supporting Information). In this paper, G70 is chosen as the representative DPE for actuation characterization and application exploration, except where otherwise noted. Moreover, the viscosity of silicone oil, one of

the DPE components, can influence the actuation performance (Figure S20, Supporting Information), the exploration of which will be our future work.

2.3. Electrode Parameters

Factors related to the electrode, including size, geometry, and structure, are important for dielectrophoretic actuation because they determine the distribution of the electric field. To optimize actuation performance with respect to electrode geometry, we investigated three important electrode parameters: the diameter of Electrode A (D_A), the inner diameter of Electrode B (D_B), and distance between Electrode A and Electrode B (D_C), via a series of experiments and finite element analyses. Because the DPE (G70 in these evaluations) is very flexible, it tends to form a concave surface under gravity when laying on ring-shaped Electrode B, and the larger the D_B , the more evident the concave shape, as explained by Figure S21 (Supporting Information). We define the plane of Electrode B as the origin of the displacement axis; therefore, the initial points of the displacement curves are negative owing to the concave shape induced by gravity. Although the thickness of the DPE sample is 1.5 mm, and therefore the maximum displacement is 1 mm when D_C is 2.5 mm, deformation of the gel may lead to a higher measured displacement (as shown in Figure 3b,e).

First, Electrode B with different inner diameters is investigated under a voltage of 3 kV when D_A (10 mm) and D_C (2.5 mm) are constant, as schematically illustrated in Figure 3a (see Figure S22a, Supporting Information for images of different Electrode B). Due to the inherent stickiness of the DPE sample, only the area suspended over the aperture of Electrode B can move, while other areas adhere to the annular section of Electrode B. As such, enlarging D_B allows more of the DPE to move, which results in larger measured deformation. For instance, in Figure 3b, the curve of smallest aperture ($D_B = 6 \text{ mm}$) shows lowest displacement. On the other hand, as illustrated by the electric field strength distribution simulation results in Figure 3c, the electric field gradient is reduced as D_B increases. The consequence is that dielectrophoresis becomes weaker, leading to poorer actuation performance, as revealed by the lowest displacement curve of $D_B = 21 \text{ mm}$ (Figure 3b). In contrast, curves of $D_B = 12, 15, \text{ and } 18 \text{ mm}$ exhibit faster actuation speed (Figure S23a, Supporting Information), and the DPE membrane is able to reach its maximum movement (1 mm) within 90 s. Particularly, a relatively fast and large displacement is observed in the curve of $D_B = 15 \text{ mm}$, moving from approximately -850 to $1000 \mu\text{m}$ in 70 s, one example of which is demonstrated in Figure S8a and Video S3a (Supporting Information).

Further, the influence of D_A was explored by using $D_B = 15 \text{ mm}$, and $D_C = 2.5 \text{ mm}$, as shown in Figure 3d (images of Electrode A are shown in Figure S22b, Supporting Information). Figure 3e illustrates the experimental results; displacement is minimal when $D_A = 5 \text{ mm}$, but becomes larger, and more rapid, with the enlargement of D_A . The curve of $D_A = 20 \text{ mm}$ reaches 1 mm displacement in 15 s with the actuation speed of $171 \mu\text{m s}^{-1}$ (Figure S23b, Supporting Information), which is the fastest movement. This result can be explained by examining the electric field (Figure 3f); the increase in D_A

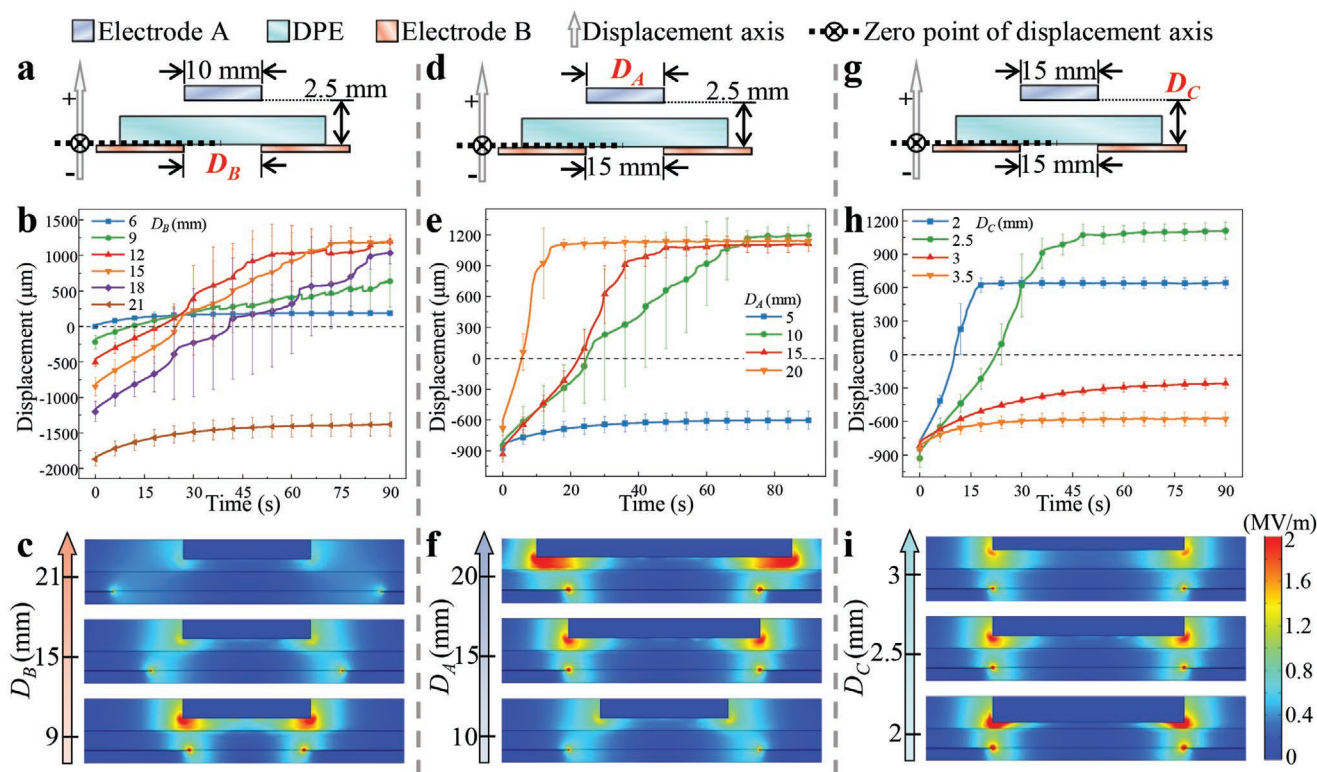


Figure 3. Experimental investigation and finite element simulation to show the influence of electrode parameters on actuation performance: a–c), d–f), and g–i) show variation of D_B (inner diameter of Electrode B), D_A (diameter of Electrode A), and D_C (distance between Electrode A and Electrode B), respectively. a,d,g) Diagram of cross-sectional view of electrode structures and used parameters. The thickness of the DPE sample was fixed at 1.5 mm. b,e,h) Experimental displacement characterization. c,f,i) Finite element simulation of electric field strength distribution. Actuation and simulation voltage was 3 kV in all cases.

increases the overlap between the two electrodes and creates a high intensity electric field around the edge of Electrode A. In doing so, strong dielectrophoretic forces emerge, leading to fast actuation. Similarly, decreasing D_C while keeping D_B (15 mm), and D_A (15 mm) constant increases actuation speed, as depicted in Figure 3g,h, and Figure S23c (Supporting Information). Compared with the low displacement when $D_C = 3.5$ mm, the curve of $D_C = 2$ mm achieves its maximum displacement of 600 μm in 20 s (Figure 3h). As can be observed in Figure 3i, reducing the distance between the electrodes results in an increase of electric field gradient, thereby generating a large dielectrophoretic actuation force.

The investigation of electrode parameters indicates that creating a high electric field gradient is important to achieving fast actuation. Because of the annular structure of Electrode B, the circular aperture area has the lowest electric field magnitude; therefore, magnifying the field around the edge of Electrode A is the most effective route to enhancing the field gradient, which could be achieved by decreasing D_C or by ensuring that D_A is always greater than D_B . However, there must be sufficient free space around the DPE for it to generate the desired displacement; for example, small D_B (6 mm) or D_C (2 mm) limits displacement (Figure 3b,h). But an overlarge D_B also has an adverse influence on actuation, as there will be a large gravitational force to overcome. In this study, a fast and large actuation stroke (1.7 mm displacement in 15 s) is observed when using geometric parameters, $D_B = 15$ mm, $D_A = 20$ mm, and $D_C = 2.5$ mm (Figure 3e). A relatively small value of D_C is a

limitation of DPE actuators in this configuration, as the upper bound of deflection is confined by D_C . If D_C is greater than 2.5 mm, the dielectrophoretic force is weak and deflection becomes small and slow (Figure 3h). Actuation speed is relatively fast when D_C is smaller than 2.5 mm, but the range of displacement is reduced. The suitable value of D_C in this paper is 2.5 mm, which means the upper bound of displacement is 1 mm (thickness of DPE is 1.5 mm). Normally, the displacement starts from about -1 mm because gravitational force can make the DPE membrane adopt a concave profile in its the initial state (Figure S21, Supporting Information). Therefore, the total displacement can reach 2 mm approximately. The influence of gravitational force on the DPE membrane should be taken into consideration when using DPE actuators. Another challenge that needs to be mentioned is the sticky nature of the DPE membrane using the presented materials. Our DPEs can stick on the Electrode A once they make contact, stopping further actuation. This, however, can be overcome through structure design or material modification.

2.4. Demonstration of Active Devices and Soft Robots Exploiting Dielectrophoretic Elastomer Actuation

2.4.1. Dielectrophoretic Elastomer Pump

The electric field-driven behavior of the DPE membrane can be exploited to develop a range of active devices and soft robots.

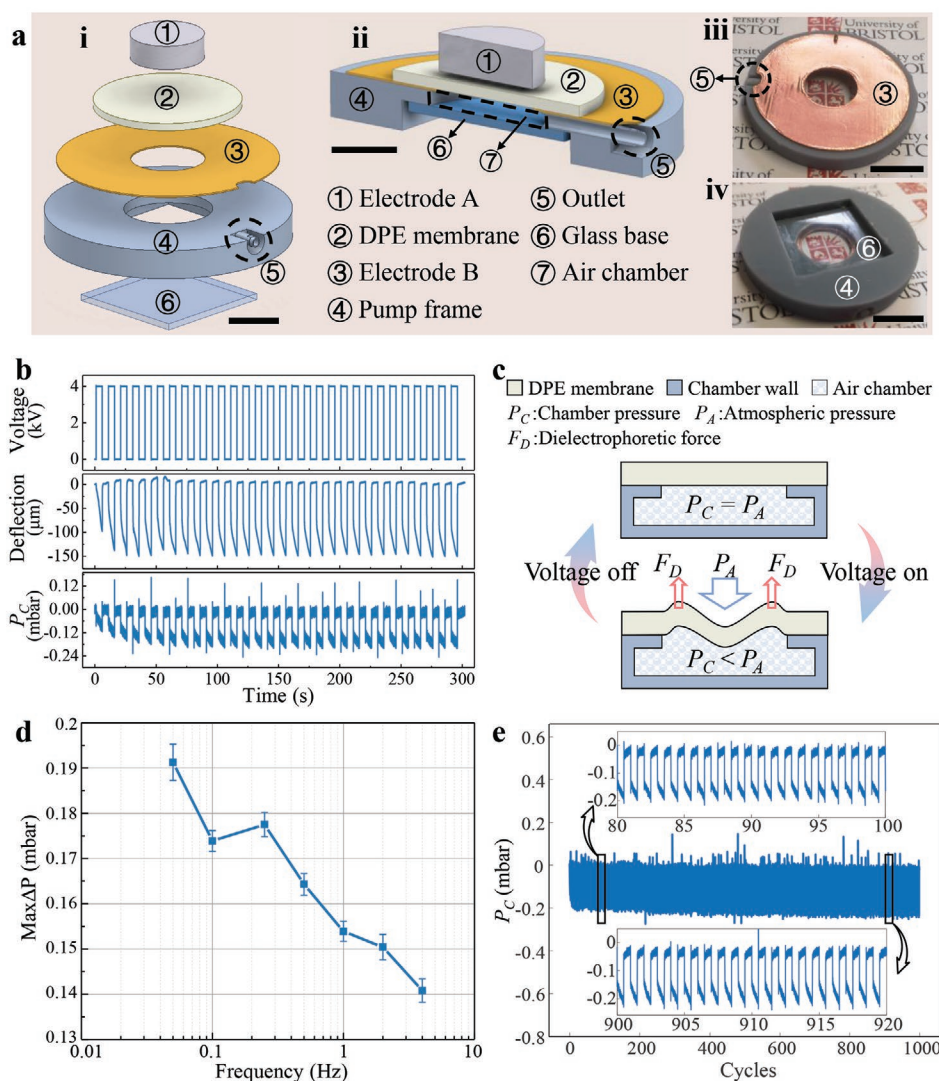


Figure 4. A pneumatic pump driven by DPE actuation. a) Exploded view (i) and cross-sectional view (ii) of a CAD model of the micropump. Photographs of the pump frame with Electrode B adhered to the top (iii) and a glass base embedded in the bottom (iv). Scale bars represent 1 cm. b) Input voltage, deflection of DPE membrane, and chamber pressure (P_C) during actuation. c) Schematic diagram of membrane deflection. d) Max ΔP at different actuation frequencies with a voltage of 4 kV. e) Cyclic test, 1000 cycles at a voltage of 4 kV and a frequency of 0.1 Hz. Inserts are enlarged views of rectangle areas.

As first proof of concept, we made a small pneumatic pump by fabricating an air chamber under a DPE actuator, as shown in **Figure 4a**. The parameters of the design are described in Table S2 (Supporting Information). A transparent glass plate (microscope coverslip) is used as the air chamber base, so that the beam of the laser displacement sensor can pass through and measure the deflection of the DPE membrane within the pump. As a demonstration, we applied 4 kV with a frequency of 0.1 Hz to the pump, with the corresponding voltage, deflection, and pressure shown in **Figure 4b**. As the DPE membrane forms the roof of the air chamber (**Figure 4a ii**), the deflection of the membrane under the application of an electric field reduces internal chamber pressure, resulting in a negative output pressure. Note that the chamber is closed and only connected to a pressure sensor. The pressure generated increases during the initial four cycles owing to the “memory” effect previously

discussed (**Figure 1g**). For all subsequent cycles, the remnant polarization reaches an equilibrium at the given frequency, and thus the output pressure generated per cycle is stable at around -0.16 mbar. Interestingly, in contrast to the results in the characterization section (where both sides of the membrane were at atmospheric pressure), the deflection of the center of the DPE pump membrane in **Figure 4b** is negative: the pump membrane always morphs downward at the center, which can be observed in **Video S4** (Supporting Information). This phenomenon stems from the pressure difference between the inside and outside of the air chamber, as shown in **Figure 4c**. The electric field around the fringe of Electrode A exhibits the strongest intensity and highest gradient, thus the DPE membrane around this area is deflected upwards according to the dielectrophoresis principle. The air volume within the chamber is expanded with the deformation of the DPE membrane, leading to the chamber

pressure (P_C) becoming smaller than atmospheric pressure (P_A). As such, atmospheric pressure squeezes the membrane, and the negative deflection appears at the center where the upward dielectrophoretic force is smaller.

The pressure performance under different working frequencies from 0.05 to 4 Hz is presented in Figure 4d. The $\text{Max}\Delta P$ is defined as the maximum pressure difference (see details in Figure S24, Supporting Information), which indicates the ability of the pump to produce pressure. As the working frequency increases, there is less time within each cycle for both membrane actuation and relaxation, so a decline of $\text{Max}\Delta P$ from 0.19 (at 0.05 Hz) to 0.14 mbar (at 4 Hz) is observed. Cyclic testing was performed for 1000 cycles under 4 kV at a frequency of 0.1 Hz. As demonstrated in Figure 4e, the output pressure over the whole testing period is stable at approximately -0.13 to -0.19 mbar, demonstrating the reliable working performance of the DPE and the pump. The DPE pump does not need any passive resistive element or external restoring force to achieve actuation, like the spring or passive layer of the dielectric elastomer actuator counterparts.^[54–56] The actuation component is only constructed by two electrodes and one elastomer membrane, which is the simplest possible pneumatic pump, and all the fabrication materials are toxic-free. The thickness of the frame and electrodes can be significantly reduced through engineering optimization and the essential thickness is only ≈ 4.5 mm in this embodiment (the air chamber and distance between electrodes, Table S2, Supporting Information). The easy fabrication, low cost ($\approx \$0.92$ US each), and thin nature of the DPE pump create an alternative solution for systems that require micro pressure control with low device complexity, such as lab-on-a-chip and microfluidic devices, and enables a wide range of future applications.

2.4.2. Dielectrophoretic Elastomer Tunable-Focus Optical Lens

The out-of-plane deflection behavior, combined with the high optically transparency of the DPE (Figure S25, Supporting Information), lend the DPE actuator to exploitation in optical systems. Here, we develop a tunable-focus optical lens using a DPE actuator, as illustrated in Figure 5a–c (parameters of the lens are depicted in Table S3, Supporting Information). Electrode A and B are integrated into the specially designed cap and base respectively (Figure S26, Supporting Information), which are easy to assemble. Electrode A is made from an indium-tin-oxide (ITO) coated polyethylene terephthalate (PET) sheet, which exhibits both electrical conductivity and high transparency. To endow the lens with better light refraction ability, a transparent dielectric liquid (silicone oil) was introduced to fill the gap between Electrode A and the DPE membrane. The working principle is shown in Figure 5d. The electrically adjustable curvature of the DPE membrane changes the profile of the lower surface of the lens, thereby significantly altering the path of light. The structure acts as a plano-convex lens at rest state (Figure 5d, upper). When a voltage is applied (4 kV as an example), the DPE membrane is deflected upward, forming a plano-concave lens (Figure 5d, lower). Typically, lenses based on dielectric elastomer actuators are double-sided convex lenses,^[57–60] and the PVC gel lens is a plano-convex

type.^[61] The tuning of focal length is achieved by changing the curvature of the convex profile. By comparison, this DPE lens can switch between convex and concave profiles, enabling a larger tuning range. The image zooming and focusing ability of the lens are demonstrated in Figure 5e,f and the accompanied Video S5 (Supporting Information). When observing a grid pattern through the lens (Figure 5e), the image of the grid is zoomed-in at electrical rest (0 kV), but can be zoomed-out during electrical activation (4 kV). The ability of the DPE lens to dynamically adjust focus is shown by observing Object A and Object B, respectively situated 12 and 70 cm from the lens (Figure 5f). At rest state (0 kV), the focus is located on the near object (Object A), thus the letter “A” is distinct. With an applied voltage (4 kV), the image of Object A becomes fuzzy, but the letter “B” becomes clear because the focus has shifted to the distant object (Object B). These results reveal the feasibility of integrating DPE actuators into optical lenses, opening a wide range of possibilities in new types of electrically adjustable imaging devices.

2.4.3. Dielectrophoretic Elastomer Walking Robot

To explore the application of DPE actuation in soft robotics, we designed a DPE actuator-driven walking robot. The robot can be divided into three functional sections: spring, body, and feet (Figure 6a), with a total mass of 1.9 g. The exploded view is depicted in Figure 6b. Two machine-cut PVC (polyvinyl chloride) films act as the frame to hold the two copper electrodes: Electrode A (round shape, diameter of 20 mm) and Electrode B (annular shape, inner diameter of 15 mm). A DPE membrane (thickness of 1.5 mm) is adhered to Electrode B, taking advantage of its inherent stickiness. The DPE actuator is therefore formed by the combination of the electrodes and the DPE membrane. To minimize the risk of a short circuit between Electrode A and B, which can occur because of their close proximity during the robot walking cycle and the higher actuation voltage used, a Kapton film is used to insulate Electrode A. The zigzag-shaped feet of the robot are bent to ensure an anisotropic friction coefficient (i.e., lower in the forward direction than in the backward direction).^[62] We also applied silicone glue on the tips of feet to increase contact friction, once dried. A steel strip (thickness of 0.04 mm) is used to join the two PVC halves of the robot due to its elasticity. The left and right PVC frames are connected to the connector and steel respectively, as indicated by thick arrows in Figure 6b. In such a system, the locomotion of the robot feet is converted into stored elastic energy in the steel strip in one half of the actuation cycle and released in the following half.

The locomotion of the DPE robot involves two stages, as demonstrated in Figure 6c and Video S6a (Supporting Information). The first stage is described as anchor-pull locomotion (Figure 6c, i to ii). When the high voltage is applied, a dielectrophoretic attraction force is generated between the DPE membrane and Electrode A. The left foot is anchored due to the larger friction; thus, the right foot is pulled leftward. In this process, the DPE is deflected toward Electrode A by dielectrophoresis, as illustrated in Figure 6d. In a control experiment, the robot did not move when we removed the DPE, indicating

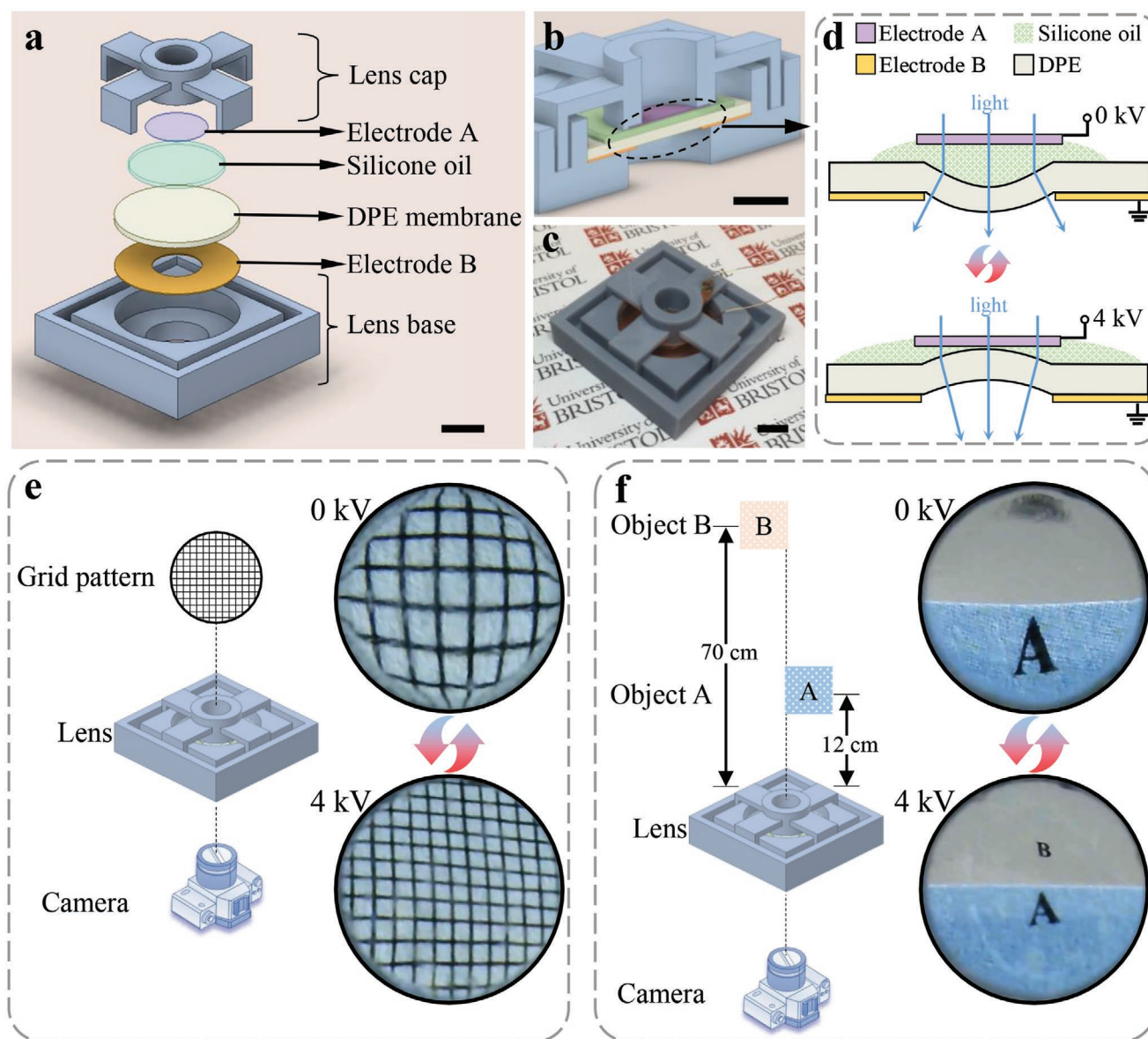


Figure 5. Design, mechanism, and demonstration of the DPE actuator as an optical lens with tunable focus. a) Exploded view and b) section view of a CAD model of the optical lens. c) A photograph of the DPE tunable lens. d) Working principle of the lens. e) Left: illustration of the active lens control setup, observing a grid pattern. Right: Images at rest state (top) and under voltage activation (bottom). The image shift from top to bottom takes ≈ 16 s. f) Left: Diagram of active focus adjustment, observing two objects at different distances. Right: Images of focus change from Object A at rest state (top) to Object B under voltage activation (bottom). The image shift from top to bottom takes ≈ 16 s. The accompanying videos of demonstration in e) and f) are available in Video S5 (Supporting Information). Scale bars in a), b), and c) represent 1 cm.

that the electrostatic force between two electrodes is not strong enough to drive the robot. In another control experiment, we replaced the DPE with a PTFE wafer (same size and thickness), which cannot be deformed by dielectrophoresis, and the robot remained stationary when energized. This means the deformation of DPE is important to locomotion. When the deflected DPE approaches Electrode A, the dielectrophoretic force between them becomes stronger. Locomotion occurs once the attraction force becomes greater than the friction. However, if the distance between the DPE and Electrode A is too close, they will stick together due to the adhesion property of the DPE. To prevent this adhesion, an end stop is introduced at the rear

foot, as shown in the inset of Figure 6b). The second stage of the gait cycle is anchor-push locomotion (Figure 6c, ii to iii). In this stage, the voltage is switched off, leading to the removal of the attraction force between DPE and Electrode A. The steel spring is then able to release its stored elastic energy, which pushes the left foot leftward. Simultaneously, the deformed gel relaxes (Figure 6d) and is ready for the next cycle. Continuous locomotion of the robot can be achieved by repeating the process. As demonstrated in Figure 6e and the accompanied Video S6b (Supporting Information), the speed of the DPE robot is 0.8 mm s^{-1} at an actuation voltage of 5 kV and a frequency of 1 Hz. Additionally, the DPE actuator integrated robot

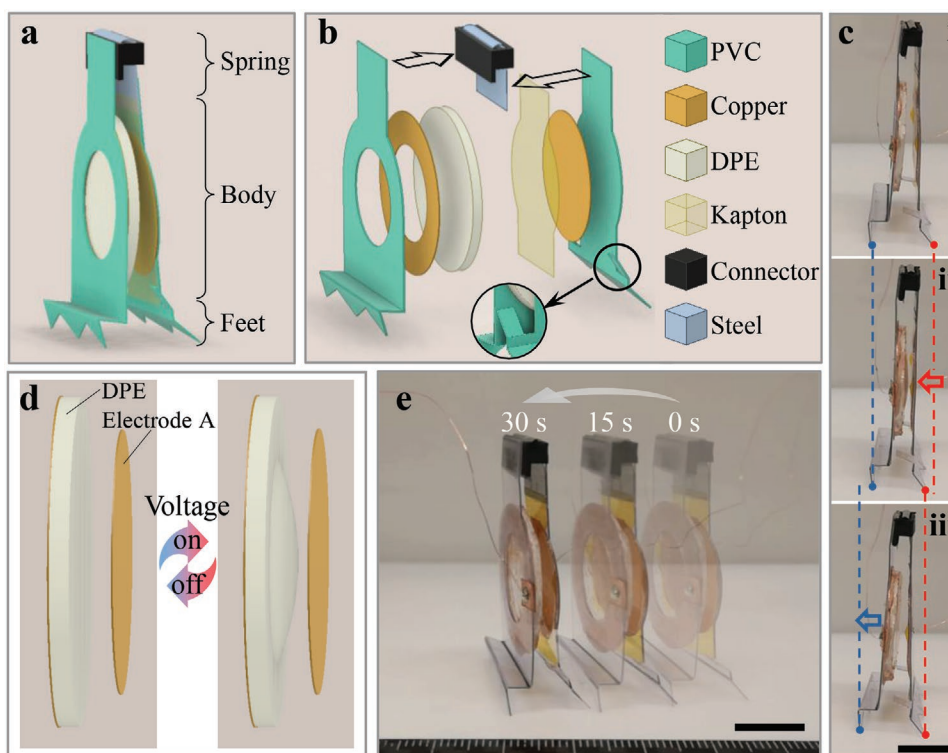


Figure 6. Design, gait, and locomotion of the DPE walking robot. a) The front view and b) exploded view of a CAD model of the robot. The insert in b) is a magnification of the end stop, which is used to prevent the complete closure of the feet. c) Walking gait of the robot. d) Deflection of DPE membrane during actuation. e) Locomotion demonstration, under an actuation voltage of 5 kV and frequency of 1 Hz. Scale bars in c) and e) represent 1 cm.

has a simple electrode configuration, and the current that flows through the system remains very small (mA), which is beneficial to thermal management in future applications.

3. Conclusion

This paper introduces a novel dielectrophoretic elastomer actuator that exhibits electric field-driven deflection due to induced dielectrophoretic forces. In contrast to other electrostatic actuation mechanisms, actuation of the DPE is dependent on the electric field intensity gradient and no direct electrode contact is needed. We present the evaluation and analysis of the dielectric and mechanical properties of a range of DPE materials with different silicone oil content. When the oil ratio reaches 70 wt.%, the DPE exhibits a very low elastic modulus (11 kPa), contributing to a fast and large deflection during actuation. To guide the design of actuators, electrode parameters are investigated experimentally and combined with finite element simulation, indicating the relationship between electric field distribution and actuation performance. Owing to the capability of DPE actuators to deform out of plane, their ease of control and simple design, we developed several proof-of-concept devices, including a pneumatic pump, a dynamically tunable lens, and a walking soft robot. This work presents a new actuation material and the first demonstration of controlled dielectrophoresis in novel gel actuators, thereby enriching the diversity of electroactive polymers and creating an alternative solution for actuation. It is envisaged that this novel approach will enable

a wider range of applications in soft robotics and soft active devices.

4. Experimental Section

Fabrication of DPE: Uncured silicone rubber matrix (Ecoflex Gel, Smooth-On) and silicone oil (Sigma-Aldrich, the viscosity is 50 cSt at 25 °C) were blended thoroughly in a petri dish. The mixture was cured at room temperature for 4 h after degassing for 20 min in a vacuum chamber. Ecoflex Gel contains two components – part A and part B – the mass ratio of which was fixed at 1:1 for all samples in this work. The mass ratio of Ecoflex Gel to silicone oil was varied in proportions 9:1, 7:3, 5:5, and 3:7 to prepare four different samples, referred to as G10, G30, G50, G70 respectively. In these ratios, the weight percentages of silicone oil in the samples were 10, 30, 50, and 70 wt.%. A reference sample of Ecoflex Gel was also fabricated following the abovementioned process, but without the addition of any silicone oil. The thickness of samples was controlled by curing a certain mass of precursor in a plastic petri dish of known dimensions, as the density of components was known (0.98 g cm⁻³ to Ecoflex Gel, 0.96 g cm⁻³ to silicone oil). The thickness of samples was checked by a laser displacement meter (LK-G402, Keyence, Japan). The thickness of all prepared samples was 1.5 mm unless otherwise specified.

Actuation and Deflection Characterization: Each Electrode A was made of aluminum rod of the specified diameter, with ends polished before use. Each Electrode B was fabricated from a bilayer sheet, consisting of a self-adhesive copper foil layer (AT525, ADVANCE, thickness of 0.35 μm) bonded to a PVC layer (thickness of 240 μm). The annular shape was obtained via a computer controlled cutting machine (Cricut Maker, Cricut, USA). In this testing set-up, Electrode B was placed on a platform with a vertical linear stage, and Electrode A was fixed over Electrode B after calibrating the plane surface of Electrode A parallel

to Electrode B. The distance between the electrodes was controlled by the linear stage and monitored by a laser displacement meter (LK-G402, Keyence, Japan) with an accuracy of $\pm 15 \mu\text{m}$. The voltage of electrodes was applied through a high voltage control system, which was composed of a high voltage amplifier (5HVA24-BP1, UltraVolt, USA), a data acquisition device (NI USB-6229, National Instruments, USA), and a PC running MATLAB. All test data, including voltage, current and displacement, were collected by the system with a sampling frequency of 1000 Hz unless otherwise specified. The deflection of the membrane was measured by a laser displacement meter (LK-G402, Keyence, Japan). As samples are transparent, a disc of paper was placed (diameter of 1.5 mm and thickness of $80 \mu\text{m}$) in the bottom center surface of the sample to act as an opaque marker for the laser beam. The curves in Figure 2f and Figure 3b,e,h were the average values with standard deviations based on at least five repeated tests. The interval between each test was at least 60 s to remove any inter-test effects.

Dielectric Property: The dielectric constants of the DPE samples were investigated using a precision LCR meter (E4980AL, Keysight, USA) with 16098B fixture and parallel electrodes (diameter of 20 mm) at ambient temperature in the frequency range of 1 to 100 kHz. The dielectric constant (ϵ') was obtained from the equation $\epsilon' = (C_p \times T) / (\epsilon_0 \times S)$, where C_p is the measured capacitance, T is the thickness of samples ($\approx 1 \text{ mm}$), ϵ_0 is the vacuum dielectric constant ($8.85 \times 10^{-12} \text{ F m}^{-1}$), and S was the area of the electrode. Each test was repeated three times.

Electrical Breakdown Strength Test: The specimens were sandwiched between two rod electrodes (20 mm diameter). The applied DC voltage, provided by high voltage amplifiers (10HVA24-BP1, UltraVolt, USA), was increased with the speed of 500 V s^{-1} until a short circuit was measured. Twelve specimens were tested for each sample. The characteristic breakdown strength was analyzed using a two-parameter Weibull statistical model described by $P = 1 - 1/\exp((E/E_b)^\beta)$, where P was the cumulative probability of electric failure, E was the experimentally measured breakdown strength of each specimen, E_b was the characteristic breakdown strength (also called scale parameter), representing the electric field up to which 63.2% (that is $1 - 1/e$ where e was the exponential constant) of the specimens breakdown, β was the shape parameter corresponding to the slope of the $\log[-\ln(1/(1-P))]$ versus $\log E$ curves. In the statistical analysis process, the experimental breakdown strength E_i was ranked in order from smallest to largest and assigned a rank i (from $i = 1$ to $i = n$, where n was the total number of tested specimens). According to the IEEE Std 930–2004 standard, the cumulative breakdown probability P_i was calculated for each E_i using the relationship: $P_i = (i - 0.44) / (n + 0.25)$.

Tensile Test: Specimens for the tensile test were prepared as dumbbell-shaped according to the ASTM D638-14 Type IV standard, with the gauge length of 25 mm, gauge width of 6 mm, and uniform thickness of 4 mm. A universal testing machine (HY-UT-5 PC, Dong Guan Hongjin test instrument co., Ltd, China) with a 10 N loading cell was used to conduct the test. The displacement rate was set as 100 mm min^{-1} . Three specimens were tested for each sample and results were reported as average and standard deviation. The Young's modulus was obtained from the secant modulus at 5% strain. Further details of the tensile test were shown in Figure S14 (Supporting Information). Moreover, two types of displacement in the tensile test were compared in Figure S15 (Supporting Information), providing guidance for the tensile test of soft gel materials.

Peeling Test: The test was conducted using a universal testing machine (HY-UT-5 PC, Dong Guan Hongjin test instrument co., Ltd, China). Various testing substrates were fixed on a sliding platform, which offset the force in the horizontal direction and maintained a peeling angle of 90° . The testing sample was fabricated as a rectangular shape of size $90 \times 30 \times 3 \text{ mm}$. One side of the sample contacted the testing substrate with the initial area of $30 \times 30 \text{ mm}$, while another side was fixed to the testing machine with a gel clamp. A Kapton film was adhered to the back of samples to prevent excessive stretching during the test. A vertical

peeling force was applied with a speed of 30 mm min^{-1} . The adhesive strength was calculated by dividing the maximum measured peeling force by the width of the sample.

Fabrication and Characterization of DPE Pump: The pump frame was fabricated using a 3D printer (Photon Mono X, Anycubic, China) and standard photopolymer resin (ELEGOO). Fabrication of Electrode A and Electrode B followed the procedure in *Actuation and Deflection Characterization*. The output pressure was measured by a differential pressure sensor (SSC010MDAA5, Honeywell, USA). A laser displacement meter (LK-G402, Keyence, Japan) was used to measure the deflection of the DPE membrane. An opaque marker (diameter of 1.5 mm and thickness of 0.2 mm) was placed on the bottom center surface of the DPE membrane for laser beam detection. In the cyclic test (Figure 4e), the reported pressure was processed by a lowpass filter function in MATLAB with a normalized passband frequency of $0.5 \pi \text{ rad sample}^{-1}$.

Fabrication of DPE Lens: The lens base and cap were 3D printed via a 3D printer (Photon Mono X, Anycubic, China) and standard photopolymer resin (ELEGOO). Electrode A was made by cutting an indium-tin-oxide (ITO) coated polyethylene terephthalate (PET) sheet (Sigma–Aldrich) to a circular shape. Electrode B was fabricated from annular-shaped bilayer sheet (following *Actuation and Deflection Characterization*). The silicone oil (viscosity 50 cSt at 25°C , refractive index 1.403 at 20°C) was purchased from Sigma–Aldrich.

Fabrication of Walking Robot: The PVC film (thickness of 0.24 mm) for the robot frame was fabricated by a computer controlled cutting machine (Cricut Maker, Cricut, USA). The connector was 3D printed (Mega S, Anycubic, China) from PLA (polylactic acid) filament. The PVC frame was attached to the connector via double sided tape.

Finite Element Analysis: The voltage and electric field strength distribution were simulated using the software COMSOL Multiphysics 5.6. The materials of Electrode A, Electrode B, and surrounding environment were simulated as Aluminum, Copper, and Air, respectively. The parameters of their relative permittivity were all used as 1. The relative permittivity of the DPE was specified as 2.8. The thickness of DPE sample and Electrode B were set as 1.5 and 0.035 mm, respectively.

Supporting Information

Supporting Information is available from the Wiley Online Library or from the author.

Acknowledgements

J.R. was supported by Engineering and Physical Sciences Research Council grants EP/R02961X/1, EP/S026096/1, EP/V062158/1, EP/V026518/1 and EP/T020792/1, and the Royal Academy of Engineering through the Chair in Emerging Technologies scheme, grant CiET1718\22. C.F.J.F. acknowledges support from the EPSRC grant EP/T020792/1. C.X. acknowledges support from the China Scholarship Council grant 202006220030.

Conflict of Interest

The authors declare no conflict of interest.

Data Availability Statement

The data that support the findings of this study are openly available in University of Bristol Research Data Repository at <https://doi.org/10.5523/bris.239k7m1nddrq72vaxbsfs2mf8>, reference number [63].

Keywords

dielectric gels, dielectrophoresis, electroactive elastomers, electroactive polymers, soft actuators

Received: August 3, 2022

Revised: November 14, 2022

Published online: February 5, 2023

- [1] J. M. McCracken, B. R. Donovan, T. J. White, *Adv. Mater.* **2020**, *32*, 1906564.
- [2] G. M. Whitesides, *Angew. Chem., Int. Ed.* **2018**, *57*, 4258.
- [3] D. Rus, M. T. Tolley, *Nature* **2015**, *521*, 467.
- [4] C. Laschi, B. Mazzolai, M. Cianchetti, *Sci. Rob.* **2016**, *1*, eaah3690.
- [5] M. Ilami, H. Bagheri, R. Ahmed, E. O. Skowronek, H. Marvi, *Adv. Mater.* **2021**, *33*, 2003139.
- [6] Y. Bar-Cohen, I. A. Anderson, *Mech. Soft. Mater.* **2019**, *1*, 5.
- [7] T. Helps, M. Taghavi, J. Rossiter, *Smart Mater. Struct.* **2019**, *28*, 085001.
- [8] Y. Qiu, E. Zhang, R. Plamthottam, Q. Pei, *Acc. Chem. Res.* **2019**, *52*, 316.
- [9] R. Pelrine, R. Kornbluh, Q. Pei, J. Joseph, *Science* **2000**, *287*, 836.
- [10] J. Shintake, S. Rosset, B. Schubert, D. Floreano, H. Shea, *Adv. Mater.* **2016**, *28*, 231.
- [11] Y. Chen, H. Zhao, J. Mao, P. Chirarattananon, E. F. Helbling, N.-s. P. Hyun, D. R. Clarke, R. J. Wood, *Nature* **2019**, *575*, 324.
- [12] X. Ji, X. Liu, V. Caciucio, M. Imboden, Y. Civet, A. El Haitami, S. Cantin, Y. Perriard, H. Shea, *Sci. Rob.* **2019**, *4*, eaaz6451.
- [13] G. Li, X. Chen, F. Zhou, Y. Liang, Y. Xiao, X. Cao, Z. Zhang, M. Zhang, B. Wu, S. Yin, Y. Xu, H. Fan, Z. Chen, W. Song, W. Yang, B. Pan, J. Hou, W. Zou, S. He, X. Yang, G. Mao, Z. Jia, H. Zhou, T. Li, S. Qu, Z. Xu, Z. Huang, Y. Luo, T. Xie, J. Gu, et al., *Nature* **2021**, *591*, 66.
- [14] M. Taghavi, T. Helps, J. Rossiter, *Sci. Rob.* **2018**, *3*, eaau9795.
- [15] E. Acome, S. K. Mitchell, T. G. Morrissey, M. B. Emmett, C. Benjamin, M. King, M. Radakovitz, C. Keplinger, *Science* **2018**, *359*, 61.
- [16] N. Kellaris, V. Gopaluni Venkata, M. Smith Garrett, K. Mitchell Shane, C. Keplinger, *Sci. Rob.* **2018**, *3*, eaar3276.
- [17] F. Hartmann, L. Penkner, D. Danning, N. Arnold, M. Kaltenbrunner, *Adv. Sci.* **2021**, *8*, 2003104.
- [18] I. D. Sirbu, G. Moretti, G. Bortolotti, M. Bolignari, S. Diré, L. Fambri, R. Vertechy, M. Fontana, *Sci. Rob.* **2021**, *6*, eaaz5796.
- [19] R. S. Diteesawat, T. Helps, M. Taghavi, J. Rossiter, *Sci. Rob.* **2021**, *6*, eabc3721.
- [20] T. Helps, C. Romero, M. Taghavi, T. Conn Andrew, J. Rossiter, *Sci. Rob.* **2022**, *7*, eabi8189.
- [21] E. Leroy, R. Hinchet, H. Shea, *Adv. Mater.* **2020**, *32*, 2002564.
- [22] W. Hu, G. Z. Lum, M. Mastrangeli, M. Sitti, *Nature* **2018**, *554*, 81.
- [23] N. El-Atab, R. B. Mishra, F. Al-Modaf, L. Joharji, A. A. Alsharif, H. Alamoudi, M. Diaz, N. Qaiser, M. M. Hussain, *Adv. Intell. Syst.* **2020**, *2*, 2000128.
- [24] Y. Kim, X. Zhao, *Chem. Rev.* **2022**, *122*, 5317.
- [25] H. A. Pohl, *J. Appl. Phys.* **1951**, *22*, 869.
- [26] H. A. Pohl, *J. Appl. Phys.* **1958**, *29*, 1182.
- [27] R. Pethig, *Biomicrofluidics* **2010**, *4*, 022811.
- [28] T. B. Jones, in *Electromechanics of Particles*, Cambridge University Press, Cambridge, **1995**, p. 34.
- [29] R. Pethig, *J. Electrochem. Soc.* **2016**, *164*, B3049.
- [30] M. Taghavi, M. Bahrami, *Mol. Simul.* **2011**, *37*, 865.
- [31] R. Pethig, in *Dielectrophoresis: Theory, Methodology and Biological Applications*, John Wiley & Sons, Ltd, Hoboken **2017**, pp. 1–29.
- [32] B. Çetin, D. Li, *Electrophoresis* **2011**, *32*, 2410.
- [33] Z. R. Gagnon, *Electrophoresis* **2011**, *32*, 2466.
- [34] R. Pethig, *Adv. Drug Delivery Rev.* **2013**, *65*, 1589.
- [35] C.-C. Cheng, C. Alex Chang, J. Andrew Yeh, *Opt. Express* **2006**, *14*, 4101.
- [36] H. Ren, H. Xianyu, S. Xu, S.-T. Wu, *Opt. Express* **2008**, *16*, 14954.
- [37] D. Hermanson Kevin, O. Lumsdon Simon, P. Williams Jacob, W. Kaler Eric, D. Velev Orlin, *Science* **2001**, *294*, 1082.
- [38] S. O. Lumsdon, D. M. Scott, *Langmuir* **2005**, *21*, 4874.
- [39] F. Krisnadi, L. L. Nguyen, Ankit, J. Ma, M. R. Kulkarni, N. Mathews, M. D. Dickey, *Adv. Mater.* **2020**, *32*, 2001642.
- [40] E. Hajiesmaili, E. Khare, A. Chortos, J. Lewis, D. R. Clarke, *Extreme Mech. Lett.* **2019**, *30*, 100504.
- [41] S. Shian, K. Bertoldi, D. R. Clarke, *Adv. Mater.* **2015**, *27*, 6814.
- [42] E. Hajiesmaili, D. R. Clarke, *Nat. Commun.* **2019**, *10*, 183.
- [43] Z. Suo, *Acta Mech. Solida Sin.* **2010**, *23*, 549.
- [44] X. Wang, X.-B. Wang, P. R. C. Gascoyne, *J. Electrostat.* **1997**, *39*, 277.
- [45] C. Rosales, K. M. Lim, *Electrophoresis* **2005**, *26*, 2057.
- [46] N. Abd Rahman, F. Ibrahim, B. Yafouz, *Sensors* **2017**, *17*, 449.
- [47] R. Pethig, in *Dielectrophoresis: Theory, Methodology and Biological Applications*, John Wiley & Sons, Ltd, Hoboken **2017**, p. 119.
- [48] P. Won, K. K. Kim, H. Kim, J. J. Park, I. Ha, J. Shin, J. Jung, H. Cho, J. Kwon, H. Lee, S. H. Ko, *Adv. Mater.* **2021**, *33*, 2002397.
- [49] S. I. Rich, R. J. Wood, C. Majidi, *Nat. Electron.* **2018**, *1*, 102.
- [50] S. M. Mirvakili, I. W. Hunter, *Adv. Mater.* **2018**, *30*, 1704407.
- [51] T. N. Do, H. Phan, T.-Q. Nguyen, Y. Visell, *Adv. Funct. Mater.* **2018**, *28*, 1800244.
- [52] L. Zhu, Q. Wang, *Macromolecules* **2012**, *45*, 2937.
- [53] J. Guo, J. Leng, J. Rossiter, *IEEE Trans. Robot.* **2020**, *36*, 313.
- [54] Z. Li, J. Zhu, C. C. Foo, C. H. Yap, *Appl. Phys. Lett.* **2017**, *111*, 212901.
- [55] P. Linnebach, G. Rizzello, S. Seelecke, *Smart Mater. Struct.* **2020**, *29*, 075021.
- [56] F. A. Mohd Ghazali, C. K. Mah, A. AbuZaiter, P. S. Chee, M. S. Mohamed Ali, *Sens. Actuator A Phys.* **2017**, *263*, 276.
- [57] F. Carpi, G. Frediani, S. Turco, D. De Rossi, *Adv. Funct. Mater.* **2011**, *21*, 4152.
- [58] J. Li, Y. Wang, L. Liu, S. Xu, Y. Liu, J. Leng, S. Cai, *Adv. Funct. Mater.* **2019**, *29*, 1903762.
- [59] S. Shian, R. M. Diebold, D. R. Clarke, *Opt. Express* **2013**, *21*, 8669.
- [60] D. Wirthl, R. Pichler, M. Drack, G. Kettlhuber, R. Moser, R. Gerstmayr, F. Hartmann, E. Bradt, R. Kaltseis, C. M. Siket, S. E. Schausberger, S. Hild, S. Bauer, M. Kaltenbrunner, *Sci. Adv.* **3**, e1700053.
- [61] J. W. Bae, E.-J. Shin, J. Jeong, D.-S. Choi, J. E. Lee, B. U. Nam, L. Lin, S.-Y. Kim, *Sci. Rep.* **2017**, *7*, 2068.
- [62] C. Cao, R. S. Diteesawat, J. Rossiter, A. T. Conn, in *2nd IEEE Int. Conf. on Soft Robotics (RoboSoft)*, **2019**, 840.
- [63] University of Bristol webpage, Data for AFM dielectrophoretic gel, <https://doi.org/10.5523/bris.239k7m1nddrq72vaxbsfs2mf8>.